Applied Numerical Mathematics 152 (2020) 511–526

Contents lists available at ScienceDirect

Applied Numerical Mathematics

www.elsevier.com/locate/apnum

Optimal explicit Runge-Kutta methods for compressible Navier-Stokes equations

V. Citro [a,*], F. Giannetti [a], J. Sierra [b]

[a] *Department of Industrial Engineering (DIIN), University of Salerno, Fisciano, 84084, Italy*
[b] *Institut de Mécanique des Fluides de Toulouse (IMFT), Toulouse, 31400, France*

ARTICLE INFO

Article history:
Received 9 August 2019
Received in revised form 7 November 2019
Accepted 7 November 2019
Available online 13 November 2019

Keywords:
Explicit Runge Kutta
Finite element method
Optimization
Stability

ABSTRACT

We focus our attention on the numerical simulations of compressible flows obtained by using Finite Difference in time /Finite Element in space approximation. In particular, we determine optimal explicit Runge-Kutta methods capable to maximize the stability features of the resulting numerical scheme. Two different regimes characterized by low and moderate Mach numbers have been taken into account. In the former regime, we have determined an explicit Runge-Kutta method of fourth order that is approximately 15% more efficient than classical ERK(4, 4) schemes. For moderate Mach numbers, $Ma \approx 0.4$, and transitional Reynolds numbers we have determined ERK schemes that outperform classic ERK(3, 3) or ERK(4, 4). Optimal ERK have a reduced CFL approximatively four or five times larger than classical ones. These optimized ERK schemes are then promising for the study of transitional flows for global stability or transient growth analyses.

1. Introduction

Integration of time dependent partial differential equations (PDE) having large separation of scales is an arduous task. On one side, three dimensional or even two dimensional discretizations of PDE leads to large set of Differential Algebraic Equations (DAE) to be solved. On the other side, the application of the method of lines to such PDEs provides stiff systems of equations. Integration of such DAE with explicit methods requires extremely small time steps in order to ensure stability of the numerical method and accuracy of the results. A wide family of implicit methods, i.e. Backward Differentiation Formula (BDF) methods, does not impose such strict requirements on the time step but requires the resolution of a general nonlinear problem at each time step. The resolution of such nonlinear problem is commonly carried out via a Newton-Krylov method, where the linear system is solved through a Krylov algorithm. Iterative methods are in fact required for three-dimensional problems since the resulting linear system is huge and complete LU factorization of the Jacobian is no longer feasible in terms of both memory and computing time. However, the performance of iterative methods is dictated by the spectra and pseudo-spectra of the discretization operator with the presence of different scales usually leading to convergence difficulties [40]. Preconditioning or accelerating techniques are a good practice and for large systems become unavoidable [9], [27], [5]. However, preconditioning is case dependent and highly related to the physics of the problem. Explicit Runge-Kutta (ERK) schemes are commonly used for time integration of large-scale spatial discretizations of partial differential equations. High-order RK methods are subjected to vast number of order conditions but they tend to have good stability properties compared to multi-step methods, as for example Adams-Bashforth numerical schemes. In the case of

* Corresponding author.
E-mail address: vcitro@unisa.it (V. Citro).

https://doi.org/10.1016/j.apnum.2019.11.005

sufficiently smooth nonlinear PDE, convergence can be proven if the method is consistent and stable [39]. However, in the presence of discontinuous solutions, which often arises in the solution of hyperbolic conservation laws, as for example Euler equations, linear stability theory is not sufficient and strong stability preserving (SSP) methods are required [21] [34]. In this article we limit the analysis to the compressible Navier-Stokes equations at low Mach numbers, so that SSP property is not required for the time integration scheme. Either stability or accuracy may constrain the temporal integration step, thus requiring more evaluations of the operator obtained from the spatial discretization of the PDE. Performance of explicit methods is usually assessed in terms of the number of required operations, which is approximated by the number of evaluations of such operator. Here, we minimize the number of function evaluations in those cases where stability is the limiting factor while preserving the order of accuracy. In Section 2 we review the classical Finite Element formulation, which is the spatial discretization considered in this article. Section 3 covers basic definitions of explicit Runge-Kutta methods and the methodology used to determine optimal stability regions. In Section 4 we describe the benchmark design case we use to determine optimal ERK methods. Fixing a configuration, we fix the spectrum of the spatial operator for a given spatial discretization. Finally in Section 5 some numerical experiments are carried out to show the effectiveness of the proposed methodology.

2. Finite element discretization

In the current section, we give a short overview of the finite element method (FEM).

2.1. Abstract setting

Consider a general quasilinear partial differential equation defined over a regular domain $\Omega \subset \mathbb{R}^3$ with boundary conditions set on its boundary $\partial\Omega$,

$$\mathbf{M}\frac{d}{dt}\mathbf{U}(\mathbf{x},t) = \sum_{ij}\mathbf{A}^{ij}_{x_i x_j}(\mathbf{U}(\mathbf{x},t)) + \sum_i \mathbf{B}^i_{x_i}(\mathbf{U}(\mathbf{x},t)) + \mathbf{f}(\mathbf{x},t,\mathbf{U}(\mathbf{x},t)) \qquad \text{in} \quad \Omega \tag{1a}$$

$$\mathbf{U}(\mathbf{x},t_0) = \mathbf{U}_0(\mathbf{x}) \qquad \text{in} \quad \Omega \tag{1b}$$

$$k_1\mathbf{U}|_{\partial\Omega} + k_2\frac{\partial \mathbf{U}}{\partial n}|_{\partial\Omega} = \mathbf{U}(\mathbf{x},t) \qquad \text{on} \quad \partial\Omega \tag{1c}$$

Here, $\mathbf{M}$ is the mass matrix of the first order differential term in time, $\mathbf{A}^{ij}_{x_i x_j}$ and $\mathbf{B}^i_{x_i}$ are a second and first order differential terms in space and $\mathbf{f}$ is a source term function (linear or a power function in $\mathbf{U}$). The coefficients k_1 and k_2 are chosen in order to set appropriate Dirichlet, Neumann or Robin boundary conditions. The finite element approximation is derived from the variational formulation of Eq. (1). Consider an initial condition $\mathbf{U}_0(\mathbf{x}) \in [L^2(\Omega)]^n$, where n is the number of variables of the PDE system and a Hilbert space $H(\Omega)$, defined in such a way that boundary conditions (Eq. (1c)) are satisfied. The variational formulation can be written as follows:

$$\begin{aligned}&\langle \mathbf{M}\frac{d}{dt}\mathbf{U}(\mathbf{x},t),\mathbf{V}\rangle_{H(\Omega)} + \sum_{ij}\langle \mathbf{A}^{ij}_{x_j}(\mathbf{U}(\mathbf{x},t)),\partial_{x_i}\mathbf{V}\rangle_{H(\Omega)} - \langle\sum_i \mathbf{B}^i_{x_i}(\mathbf{U}(\mathbf{x},t)),\mathbf{V}\rangle_{H(\Omega)}\\ &-\langle \mathbf{f}(\mathbf{x},t,\mathbf{U}(\mathbf{x},t)),\mathbf{V}\rangle_{H(\Omega)} - \sum_{ij}\langle \mathbf{A}^{ij}_{x_j}(\mathbf{U}(\mathbf{x},t)),\mathbf{V}\rangle_{H(\partial\Omega)} = 0 \qquad \text{in} \quad \Omega\end{aligned} \tag{2}$$

where $\mathbf{V} \in L^2(0,T;H)$ and $\frac{d}{dt}\mathbf{V} \in L^2(0,T;H)$. Equation (2) can be conveniently written as follows:

$$\begin{aligned}&\langle \mathbf{M}\frac{d}{dt}\mathbf{U}(\mathbf{x},t),\mathbf{V}\rangle_{H(\Omega)} + \underbrace{a(\mathbf{U},\mathbf{V})}_{\sum_{ij}\langle \mathbf{A}^{ij}_{x_j}(\mathbf{U}(\mathbf{x},t)),\partial_{x_i}\mathbf{V}\rangle_{H(\Omega)}} + \underbrace{b(\mathbf{U},\mathbf{V})}_{-\langle\sum_i \mathbf{B}^i_{x_i}(\mathbf{U}(\mathbf{x},t)),\mathbf{V}\rangle_{H(\Omega)}}\\ &+ \underbrace{c(\mathbf{U},\mathbf{V})}_{-\langle \mathbf{f}(\mathbf{x},t,\mathbf{U}(\mathbf{x},t)),\mathbf{V}\rangle_{H(\Omega)}} + \underbrace{f(\mathbf{V})}_{-\sum_{ij}\langle \mathbf{A}^{ij}_{x_j}(\mathbf{U}(\mathbf{x},t)),\mathbf{V}\rangle_{H(\partial\Omega)}} = 0\end{aligned} \tag{3}$$

The problem therefore can be stated as

$$\text{find } \mathbf{U} \in W(0,T) = \left\{\mathbf{V} \in L^2(0,T;H),\ \frac{d}{dt}\mathbf{V} \in L^2(0,T;H)\right\} \quad \text{for a.e. } t \in (0,T) \quad : (\text{Eq. } (3)) \tag{4}$$

We remark that formulation (4) has a meaning due to the compact embedding of $W(0,T)$ into $\mathcal{C}^0([0,T];H)$, so that the initial condition $\mathbf{U}_0$ has a meaning in $H(\Omega)$. Please note that in the previous example we have considered problem described by the bilinear forms a and b. Non-linear PDEs, such as Navier-Stokes equations (Eq. (28)), in addition to bilinear forms, require the introduction of trilinear forms such as $\eta(\mathbf{U},\mathbf{V},\mathbf{W})$. However, the procedure to derive discretized finite element operators is essentially the same as in the linear case. Please consider [32] and [33] for a more detailed study of Navier-Stokes equations and their finite element discretization.

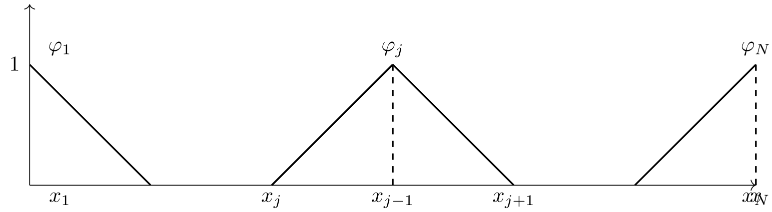

Fig. 1. Global shape functions of the space $H_h^1(\mathbb{R})$.

2.2. Semi-discretization in space

The domain $\Omega \subset \mathbb{R}^2$ is supposed to be polygonal. We define a triangulation $\mathcal{T}_h$ of Ω composed of elements K_j for $1 \leq j \leq N$ and we denote $H_h \subset H$ the finite conformal subspace associated to $\mathcal{T}_h$ of dimension N_{DoF} (see Fig. 1). The discrete version of Eq. (2) is then expressed as follows

$$\begin{aligned}&\langle \mathbf{M}\frac{d}{dt}\mathbf{U}_h(\mathbf{x},t), \mathbf{V}_h\rangle_{H_h(\Omega)} + \sum_{ij}\langle \mathbf{A}^{ij}_{x_j}(\mathbf{U}_h(\mathbf{x},t)), \partial_{x_i}\mathbf{V}_h\rangle_{H_h(\Omega)} - \langle \sum_i \mathbf{B}^i_{x_i}(\mathbf{U}_h(\mathbf{x},t)), \mathbf{V}_h\rangle_{H_h(\Omega)} \\ &- \langle \mathbf{f}(\mathbf{x},t,\mathbf{U}_h(\mathbf{x},t)), \mathbf{V}_h\rangle_{H_h(\Omega)} - \sum_{ij}\langle \mathbf{A}^{ij}_{x_j}(\mathbf{U}_h(\mathbf{x},t)), \mathbf{V}_h\rangle_{H_h(\partial\Omega)} = 0 \qquad \text{in} \quad \Omega \end{aligned} \tag{5}$$

where $\mathbf{U}_h, \mathbf{V}_h, \mathbf{U}_{0,h}$ are elements $\in H_h(\Omega)$. The problem can be thus reformulated as

$$\text{Find } \mathbf{U}_h \in W_h(0,T) = \left\{\mathbf{V}_h \in L^2(0,T;H_h), \frac{d}{dt}\mathbf{V}_h \in L^2(0,T;H_h)\right\} \quad \text{for a. e. } t \in (0,T) \quad : (\text{Eq. } (5)) \tag{6}$$

The vector functions $\mathbf{U}_h$ and $\mathbf{V}_h$ can be expressed in terms of the $H_h(\Omega)$ finite basis $\{\varphi_j(\mathbf{x})\}_{0\leq j\leq N_{DoF}}$ as

$$\mathbf{U}_h = \sum_{j=0}^{N_{DoF}} \mathbf{U}_h|_{K_j}(\mathbf{x})\varphi_j(\mathbf{x}), \quad \forall \mathbf{x} \in \Omega \tag{7}$$

$$\mathbf{V}_h = \sum_{j=0}^{N_{DoF}} \mathbf{V}_h|_{K_j}(\mathbf{x})\varphi_j(\mathbf{x}), \quad \forall \mathbf{x} \in \Omega \tag{8}$$

Since $\mathbf{V}_h|_{K_j}$ is an arbitrary test function, a general convention in FEM is to consider $\mathbf{V}_h = \sum_{j=0}^{N_{DoF}} \varphi_j(\mathbf{x})$, so that Eq. (5) is finally reformulated as a finite dimensional problem as

$$\begin{aligned}&\sum_{K_k}\Big[\mathbf{M}\frac{d}{dt}\mathbf{U}_h|_{K_k}\langle \varphi_k, \varphi_k\rangle + \mathbf{U}_h|_{K_k}\sum_{ij}\langle \mathbf{A}^{ij}_{x_j}(\varphi_k), \partial_{x_i}\varphi_k\rangle_{H_h(\Omega)} - \langle \sum_i \mathbf{B}^i_{x_i}(\varphi_k), \varphi_k\rangle_{H_h(\Omega)} \\ &- \mathbf{U}_h|_{K_k}\sum_{ij}\langle \mathbf{A}^{ij}_{x_j}(\varphi_k, \varphi_k\rangle_{H_h(\partial\Omega)}\Big] - \mathbf{f}(\sum_{K_k}\mathbf{U}_h|_{K_k})\langle \mathbf{f}(\sum_{K_k}\varphi_k), \sum_{K_k}\varphi_k\rangle_{H_h(\Omega)} = 0 \qquad \text{in} \quad \Omega \end{aligned} \tag{9}$$

2.3. Lagrange elements

Finite element methods for Lagrange $\mathbb{P}_k$ elements involve the space of globally continuous functions on each element,

$$H_h^k = \left\{\mathbf{V}_h \in \mathcal{C}^{k-1}(\Omega), \mathbf{V}_h|_{K_j} \in \mathbb{P}_k, \quad 0 \leq j \leq N \quad \text{such that boundary conditions are satisfied}\right\}$$

where the polynomial space $\mathbb{P}_k$ is defined as:

$$\mathbb{P}_k = \left\{p(x) = \sum_{j=0}^{k}\alpha_j x^j, \quad \alpha_j \in \mathbb{R}\right\}$$

3. Explicit time integration schemes

3.1. Definitions

Given an initial value problem (IVP),

$$\begin{aligned} \frac{d}{dt}\mathbf{U}(t) &= \mathbf{F}(\mathbf{U}(t)) \\ \mathbf{U}(t_0) &= \mathbf{U}_0 \end{aligned} \tag{10}$$

where $\mathbf{U}_0 \in \mathbb{R}^N$ and $\mathbf{F} \in \mathcal{C}^n(\mathbb{R}^N)$, a commonly used class of methods to solve the IVP are Explicit Runge-Kutta (ERK) schemes. A $s-$stage p-order ERK(s,p) method is characterized by a lower triangular matrix $\mathcal{A} \in \mathbb{R}^{s\times s}$, a vector $\mathbf{b} \in \mathbb{R}^s$ and a vector $\mathbf{c} \in \mathbb{R}^s$, which determine the Butcher's tableau [2]. The IVP can be recast into the Picard integral formulation

$$\mathbf{U}(t) = \mathbf{U}_0 + \int_0^t \mathbf{F}(\mathbf{U}(\tau))d\tau \tag{11}$$

Note that using a particular ERK(s,p) scheme to solve the IVP is equivalent to choose a specific quadrature formula to approximate Eq. (11). Let's indicate now with $\mathbf{U}_n$ the numerical approximation of the solution $\mathbf{U}(t)$ at time, $t = t_n$, and with $\mathbf{U}_n^i$ the numerical approximation of $y(t)$ at time $t = t_n + c_i\Delta t$, where c_i is imposed as $c_i = \sum_{j=1}^s a_{ij}$. This last equation together with the condition $\sum_{j=1}^s b_j = 1$ guarantees the consistency of the scheme. Further conditions have to be imposed to obtain a scheme of a given p order of accuracy. The continuous IVP problem (Eq. (10)) is thus formulated in discrete form as

$$\mathbf{U}_n^i = \mathbf{U}_n + \Delta t \sum_{j=1}^{i-1} a_{ij}\mathbf{F}(\mathbf{U}_n^j) \tag{12a}$$

$$\mathbf{U}_{n+1} = \mathbf{U}_n + \Delta t \sum_{i=1}^{s} b_i\mathbf{F}(\mathbf{U}_n^i) \tag{12b}$$

In the context of MOL (Methods of Lines), strong stability preserving (SSP) is a required property for a time-integration scheme whenever the space discretization vector $\mathbf{F}$ is discontinuous. In such a case, in order to prevent oscillations of the spatial discretization, different approaches have been proposed, such as limiters for the Lax-Wendroff scheme [13] or Total Variation Diminishing (TVD) schemes [4]. In order to correctly represent discontinuous solutions of a hyperbolic PDE, it is well known that the time integration scheme should posses a TVD property similar to the spatial discretization. Forward Euler scheme, for example, posses the same nonlinear property as TVD methods: it is stable in the l_∞ norm. SSP is a generalization of the TVD property to the time discretization for a wider family of higher order temporal schemes. However, whenever a given PDE admits a smooth solution, SSP property is no longer strictly needed since the vector function $\mathbf{F}$ is sufficiently smooth, $\mathbf{F} \in \mathcal{C}^n$ where $n \in \mathbb{N}$, as stated in [39, Theorem 1]. In this case convergence is a direct consequence of consistency and linear stability in the l_2 norm. Here we will treat only equations with smooth solutions so that SSP schemes will be no longer considered.

3.2. Linear stability polynomial

Linear stability in the l_2 norm (often referred as Absolute Stability) of the ERK family of methods is studied by considering a simple linear scalar problem $\frac{d\mathbf{Y}(t)}{dt} = \lambda\mathbf{Y}(t)$, where $\lambda = \lambda_r + i\lambda_i \in \mathbb{C}$. After discretization in time, any ERK method leads to the following iteration map

$$\mathbf{Y}_{n+1} = \zeta(\Delta t\lambda)\mathbf{Y}_n \tag{13}$$

where the *stability polynomial* $\zeta(z)$:

$$\zeta(z) = 1 + \sum_{j=0}^{s} \mathbf{b}^T\mathcal{A}^{j-1}\mathbf{e}z^j \tag{14}$$

depends only on the Butcher's tableau of the considered method (Eq. (12)). Here $\mathbf{e}$ is a vector column composed by ones. It is clear that the error propagation is governed by the function ζ, since at every time-step the error is amplified/reduced by a factor $\zeta(\Delta t\lambda)$. A given error, thus, will remain bounded whenever the module of the stability polynomial is lower or equal to 1. The *absolute stability region* is the set S in the complex plane where the ERK method is absolute stable, i.e. where

$$\Delta t\lambda \in S \qquad \text{where} \qquad S = \{z \in \mathbb{C} : |\zeta(z)| \le 1\} \tag{15}$$

Table 1
Dissipation order conditions [26].

p Order of accuracy	q Dissipative order	Conditions
3	3	$\beta_2 = \frac{1}{2}$, $\beta_3 = \frac{1}{6}$
3,4	5	$\beta_2 = \frac{1}{2}$, $\beta_3 = \frac{1}{6}$, $\beta_4 = \frac{1}{24}$
3,4	7	$\beta_2 = \frac{1}{2}$, $\beta_3 = \frac{1}{6}$, $\beta_4 = \frac{1}{24}$, $\beta_5 - \beta_6 = \frac{1}{144}$

Table 2
Dispersion order conditions [41].

p Order of accuracy	r Dispersive order	Conditions
2,3	4	$\beta_2 = \frac{1}{2}$, $\beta_3 = \frac{1}{6}$
2,3	6	$\beta_2 = \frac{1}{2}$, $\beta_3 = \frac{1}{6}$, $\beta_4 - \beta_5 = \frac{1}{30}$
4,5	6	$\beta_2 = \frac{1}{2}$, $\beta_3 = \frac{1}{6}$, $\beta_4 = \frac{1}{24}$

3.3. Dissipation and dispersion in ERK

We follow the approach of [26] and [41] to describe dissipation and dispersion errors (see also [31], [30]). To do so, let's consider the linear equation $\frac{d\mathbf{Y}(t)}{dt} = \lambda \mathbf{Y}(t)$, with $\lambda = \lambda_r + i\lambda_i \in \mathbb{C}$, which has the solution

$$\mathbf{Y}(t + \Delta t) = e^{\Delta t(\lambda_r + i\lambda_i)}\mathbf{Y}(t) \tag{16}$$

The approximated vector $\mathbf{Y}_{n+1}$ can be expressed with respect to the previous approximation with Albrecht's notation [1] in the form,

$$\mathbf{Y}_{n+1} = \big(1 + \Delta t\lambda \mathbf{b}^T\mathbf{e} + \ldots + (\Delta t\lambda)^s \mathbf{b}^T \mathcal{A}^{s-1}\mathbf{e}\big)\mathbf{Y}_n = \zeta(\Delta t\lambda)\mathbf{Y}_n \tag{17}$$

where $\mathbf{e} \in \mathbb{R}^s$. Let us define $\beta_j = \mathbf{b}^T\mathcal{A}^{j-1}\mathbf{e}$, then Eq. (17) can be rewritten as

$$\mathbf{Y}_{n+1} = \big(1 + \Delta t\lambda\beta_1 + \ldots + (\Delta t\lambda)^s\beta_s\big)\mathbf{Y}_n = (\zeta_r(\Delta t\lambda) + i\zeta_i(\Delta t\lambda))\mathbf{Y}_n \tag{18}$$

The ERK method is of *dissipative order* q if

$$e^{\lambda_r\Delta t} - |\zeta_r(\Delta t\lambda) + i\zeta_i(\Delta t\lambda)| \approx O(\Delta t^{q+1}) \tag{19}$$

similarly, a ERK method is of *dispersive order* r if

$$\Delta t\lambda_i - \arctan(\frac{\zeta_i(\Delta t\lambda)}{\zeta_r(\Delta t\lambda)}) \approx O(\Delta t^{r+1}) \tag{20}$$

In practical terms, the coefficients β_j for $j = 1, \ldots, p$ are fixed by order conditions of the selected ERK. Dissipative and dispersive orders impose extra conditions, see Table 1 and Table 2.

3.4. Optimization of ERK(s, p)

Explicit Runge-Kutta methods (Eq. (12)) are completely determined by their Butcher's tableau. Order conditions fix some of the degrees of freedom, i.e. some values of the matrix $\mathcal{A}$ and the vector $\mathbf{b}$. However, for high order schemes (let's consider $p \geq 3$) and a number of stages bigger than those required by order conditions, additional degrees of freedom can be tuned to determine an optimal ERK method in terms of a given cost function. In the past [29] considered the order of accuracy as a cost function for a prescribed stability contour for the 4th order RK schemes, [19] considered a similar problem for low storage SSP-RK methods whereas [26] optimized the absolute stability region for a given order of dissipation and dispersion.

In the present article we consider the minimization problem given by Eq. (21).

$$\begin{aligned}
&\underset{a_{ij}, b_i}{\text{minimize}} \Big(\sum_i \tau_i^{(p+1)}\Big)^{\frac{1}{2}} \\
&\text{subject to} \beta_j = d_j, \;\; j = p+1, \ldots, s. \\
&\qquad ||\mathbf{Y}(t) - \mathbf{Y}_n|| = O(\Delta t^p) \\
&\qquad \Delta t\lambda_i - \arctan(\frac{\zeta_i(\Delta t\lambda)}{\zeta_r(\Delta t\lambda)}) = O(\Delta t^{q+1}) \\
&\qquad e^{\lambda_r\Delta t} - |\zeta_r(\Delta t\lambda) + i\zeta_i(\Delta t\lambda)| = O(\Delta t^{r+1})
\end{aligned} \tag{21}$$

Here d_j are some prescribed values and p, q, r are fixed orders. The problem minimizes precision error for a given order of accuracy, dissipation, dispersion and a prescribed absolute stability region that covers a region of the complex plane.

Optimal absolute stability region shape for a given spectrum. In order to determine the coefficients d_j that are used in Eq. (21) we need to solve another optimization problem [28] [23] [24]. In particular given the spectrum of the semi-discrete spatial operator $\Lambda \in \mathbb{C}$ and fixed coefficients p, q, r, s, we solve

$$\underset{\beta_j}{\text{minimize}} \max_{\lambda \in \Lambda}(|\zeta(\Delta t \lambda)| - 1). \tag{22}$$

Then optimal values β_j^* are designed as d_j and then set as constraints to Problem (Eq. (21)).

Remark. We remark here that the function $|\zeta(\Delta t \lambda)|$ is proper (not identical to ∞), convex and coercive in β_j since it is a polynomial whose degree is at least one and continuous. Thus it accepts minimizer β_j for $j = p+1, \ldots, s$. Note also that Eq. (22) and Eq. (21) are constrained convex optimization problems, so that they can be solved with any classical algorithm for differentiable convex problems such as projected gradient, SQP algorithm or interior-penalty.

4. Optimal ERK for acoustic problems

In this section we describe the derivation of optimal ERK schemes in terms of stability for the compressible Navier-Stokes equations at low and moderate Mach numbers and for low to moderate Reynolds numbers. The selected methodology has been explained in Section 3.4.

4.1. Simplified model for the design of optimal ERK

The efficiency of a time integration scheme can be assessed by measuring its performances with respect to a given benchmark case. In the present article, it is desired to build efficient ERK methods for the spatial discretization of large-scale PDE problems. In particular, our interest focuses here in compressible flow simulations which are modeled by the compressible Navier-Stokes equations (Eq. (28)). The dimensionless numbers (well known in the CFD community) Re (Reynolds number) and Ma (Mach number) are quantities that characterize the dynamics of the system. Whereas Re indicates the ratio between inertial and viscous forces, Ma provides the scaling between convective and acoustic speeds. For subsonic flows, the separation of scales in the problem increases as Re gets larger and Ma decreases. In the present article we determine efficient methods for low to moderate values of Ma (i.e. $Ma \in [0.01, 0.7]$) and for values of Re corresponding to laminar or transitional regimes. In order to derive an optimal scheme we shall consider a simplified problem which possesses the main features of the full problem but for which a full determination of the spectrum of the spatial discretization is possible. Since our interest focuses on compressible Navier-Stokes equations, at subsonic regime and low to moderate Re, most of the numerical features of the full problem are already present in the linear advection-diffusion equation with the same parameters as the full problem. The choice of the linear advection-diffusion equation can be justified more rigorously. Consider the one-dimensional Euler's equations written in quasilinear form $\frac{\partial \mathbf{Q}}{\partial t} + \mathbf{A}\frac{\partial \mathbf{Q}}{\partial x} = 0$, where the conservative variable $\mathbf{Q}$ is defined as $\mathbf{Q} = [\rho, \rho u, e]^T$. Whenever one looks at small perturbations, a linearization around a base state can be performed to analyze the evolution of the perturbations. Thus, for a given state, the eigenvalues of the Jacobian matrix $\mathbf{A}_0$ are $\lambda_1 = u + c$, $\lambda_2 = u - c$ and $\lambda_3 = u$, where $c = \sqrt{\frac{\gamma p}{\rho}}$ is the speed of sound. Using the associated eigenvectors as a basis, the Euler equations can be rewritten as $\frac{\partial \mathbf{W}}{\partial t} + \mathbf{\Lambda}_0 \frac{\partial \mathbf{W}}{\partial x} = 0$ where $\mathbf{W}$ is the generalized vector of state and $\mathbf{\Lambda}$ is a diagonal matrix whose entries are the eigenvalues of $\mathbf{A}_0$. The problem is now totally decoupled and we can therefore consider only the components associated to $\lambda_1 = u + c$ and $\lambda_3 = u$. The eigenvalue $\lambda_2 = c - u$ is similar to the case $\lambda_1 = u + c$ but with opposite sign for low convective speed u. Note that here we just considered Euler's equations for simplicity, but a similar analysis can be carried out for the one-dimensional compressible Navier-Stokes equations. In such case the problem can be reduced to the study of the behavior of the following equations

$$\frac{\partial u(x,t)}{\partial t} + \left(1 + \frac{1}{Ma}\right)\partial_x u(x,t) - \frac{1}{Re}\partial_{xx} u(x,t) = 0 \tag{23a}$$

$$\frac{\partial w(x,t)}{\partial t} + \partial_x w(x,t) - \frac{1}{Re}\partial_{xx} w(x,t) = 0. \tag{23b}$$

By inspecting Eq. (23), we note the existence of two different regimes occurring whenever $1 + \frac{1}{Ma} \gg 1$ and $\frac{1}{Re} \ll 1$ or $1 + \frac{1}{Ma} \approx O(1)$ and $\frac{1}{Re} \approx O(10^{-n})$, for a small value of $n \in \mathbb{N}$, for instance $n = 2$. The first case corresponds to an advection dominated problem whereas in the second case, advection and diffusion have similar scaling. Problem (Eq. (23)) is complemented with periodic boundary conditions on a finite domain $\Omega = \mathbb{T}$.

4.2. FEM discretization

Problem (Eq. (23)) is solved numerically by using affine functions $\mathbb{P}_1$ and quadratic functions $\mathbb{P}_2$ (see Section 2.3) as finite elements basis. We have considered two different cases depending on the value of the dimensionless numbers Ma and Re.

Advection dominated case: $\frac{1}{M} \gg 1$. Whenever the Mach number is small and Re is sufficiently high, the spectrum of the discretized spatial operator is almost insensitive to diffusive effects. In such a case we consider Eq. (23a).

Advection-diffusion case: $1 + \frac{1}{Ma} \approx O(1)$ *and* $\frac{1}{Re} \approx O(10^{-n})$. In this case the spectrum of the semi-discretized operator appears to be sensitive to advection and diffusive effects. That is, it has a larger support in the negative side of the complex plane for larger negative real values. For this configuration the interesting equation to analyze is Eq. (23b).

We thus consider the spatial discretizations of the convection ∂_x and diffusion ∂_{xx} operator with $\mathbb{P}_1$ and $\mathbb{P}_2$ Lagrange elements. Below we display a $\mathbb{P}_2$ spatial discretization for a uniform one-dimensional mesh:

$$\mathbf{M} = \frac{\Delta x}{6} \begin{array}{c} \begin{array}{ccc} \mathbf{M}_{-1} & \mathbf{M}_0 & \mathbf{M}_1 \end{array} \\ \begin{pmatrix} 8 & 2 & -1 & 0 & \dots & -1 & 2 \\ 2 & 16 & 2 & 0 & \dots & 0 & 0 \\ -1 & 2 & 8 & 2 & -1 & 0 & \vdots \\ 0 & 0 & 2 & 16 & 2 & 0 & \vdots \\ \vdots & \vdots & \ddots & \ddots & \ddots & \ddots & \ddots \\ -1 & 0 & \dots & -1 & 2 & 8 & 2 \\ 2 & 0 & \dots & 0 & 0 & 2 & 16 \end{pmatrix} \end{array} \qquad \mathbf{D} = \frac{1}{6} \begin{array}{c} \begin{array}{ccc} \mathbf{D}_{-1} & \mathbf{D}_0 & \mathbf{D}_1 \end{array} \\ \begin{pmatrix} 8 & 2 & -1 & 0 & \dots & -1 & 2 \\ 2 & 16 & 2 & 0 & \dots & 0 & 0 \\ -1 & 2 & 8 & 2 & -1 & 0 & \vdots \\ 0 & 0 & 2 & 16 & 2 & 0 & \vdots \\ \vdots & \vdots & \ddots & \ddots & \ddots & \ddots & \ddots \\ -1 & 2 & 0 & \dots & 8 & 2 & -1 \\ 0 & 0 & 0 & \dots & 2 & 16 & 2 \end{pmatrix} \end{array}$$

$$\mathbf{K} = \frac{1}{3\Delta x} \begin{array}{c} \begin{array}{ccc} \mathbf{K}_{-1} & \mathbf{K}_0 & \mathbf{K}_1 \end{array} \\ \begin{pmatrix} 14 & -8 & 1 & 0 & \dots & 1 & -8 \\ -8 & 16 & -8 & 0 & \dots & 0 & 0 \\ 1 & -8 & 14 & -8 & 1 & 0 & \vdots \\ 0 & 0 & -8 & 16 & -8 & 0 & \vdots \\ \vdots & \vdots & \ddots & \ddots & \ddots & \ddots & \ddots \\ 1 & 0 & \dots & 1 & -8 & 14 & -8 \\ -8 & 0 & \dots & 0 & 0 & -8 & 16 \end{pmatrix} \end{array} \tag{24}$$

Matrices $\mathbf{M}$, $\mathbf{D}$ and $\mathbf{K}$ are the time derivative mass matrix and the convection and diffusion operator respectively. In case of periodic boundary conditions they are block Toeplitz and block circulant matrices. The matrix $\mathbf{M}$ is composed of three Toeplitz blocks $\mathbf{M}_{-1}$, $\mathbf{M}_0$ and $\mathbf{M}_1$. The other two matrices have a similar structure. The spectrum of a block Toeplitz or circular matrix coincides with the spectrum of the Fourier symbol of the block matrices composing it [25]. So, in this particular case where block Toeplitz matrices are 2×2, the spectrum of the whole discretization can be determined from a 2×2 matrix equation. Note however, that the spatial discretization of the diffusion and convection operators are not $\mathbf{D}$ and $\mathbf{K}$ but $\mathbf{M}^{-1}\mathbf{D}$ and $\mathbf{M}^{-1}\mathbf{K}$ respectively. This only adds a technical difficulty for the determination of the inverse of the mass matrix, but convective and diffusion operators are still Toeplitz block matrices, so that the procedure described above still holds: matrices are just less sparse [42].

Fig. 2 displays the spectrum of the spatial semi-discretization of the advection-diffusion equation for two different regimes: a case in which convection dominates and a case in which convection and diffusion processes have similar orders of magnitude.

Full discretization. Problem (Eq. (23)) is then fully discretized using an ERK method in time and FEM in space. In this way, we obtain for the advection-diffusion equation the following scheme

$$\mathbf{U}_n^i = \mathbf{U}_n^i + \frac{1}{6}\sum_{j=1}^{i-1} a_{ij}\Big[\frac{(1+\frac{1}{Ma})\Delta t}{\Delta x}\mathbf{M}^{-1}\mathbf{D}(\mathbf{U}_n^j) + \frac{2\Delta t}{Re\Delta x^2}\mathbf{M}^{-1}\mathbf{K}(\mathbf{U}_n^j)\Big] \tag{25a}$$

$$\mathbf{U}_{n+1}^i = \mathbf{U}_n^i + \frac{1}{6}\sum_{i=1}^{s} b_i\Big[\underbrace{\frac{(1+\frac{1}{Ma})\Delta t}{\Delta x}}_{CFL_{adv}}\mathbf{M}^{-1}\mathbf{D}(\mathbf{U}_n^j) + 2\underbrace{\frac{\Delta t}{Re\Delta x^2}}_{CFL_{diff}}\mathbf{M}^{-1}\mathbf{K}(\mathbf{U}_n^i)\Big] \tag{25b}$$

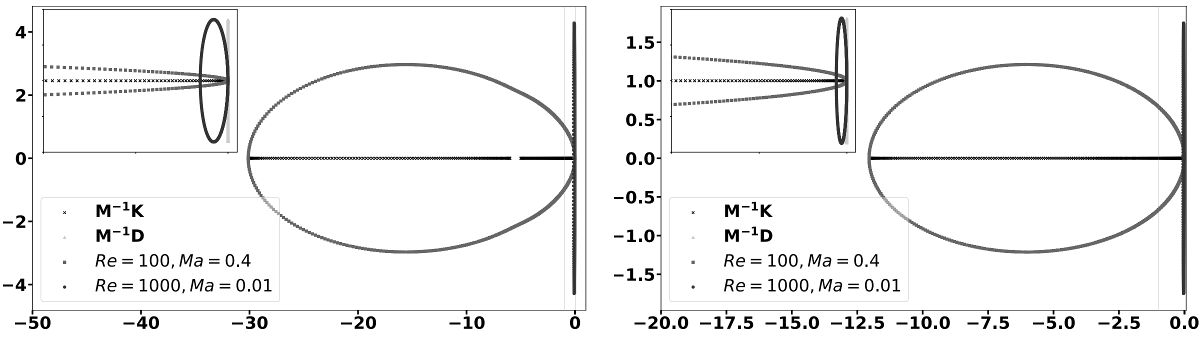

(a) $\mathbb{P}_2$ discretization (b) $\mathbb{P}_1$ discretization

Fig. 2. Spectrum of the discretized operators ∂_x, ∂_{xx} and two configurations of the advection diffusion equation.

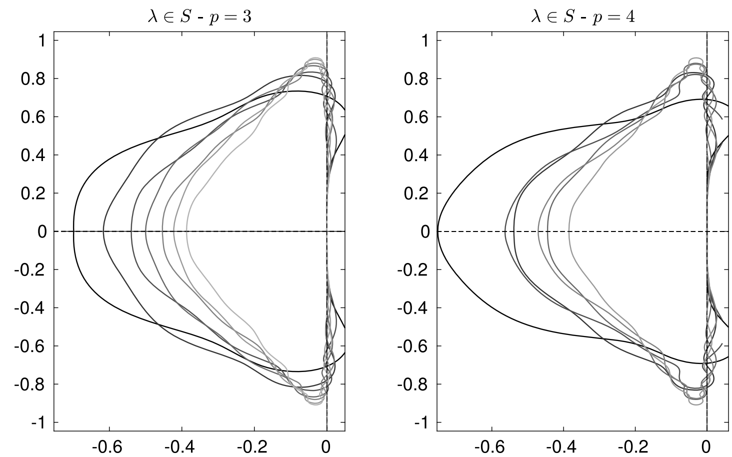

Fig. 3. *Option A*. Scaled absolute stability region with respect to the number of stages for the low Mach number case. On the left (resp. right) the stability region for several ERK schemes of order $p = 3$ (resp. $p = 4$) is displayed. Different contours correspond to schemes with different number of stages $s = [p + 1, 10]$, with lighter gray scale used for higher values of s. Dot-dashed curves correspond to the designed spectrum which corresponds to the low Mach spectrum displayed at Fig. 2.

In Eq. (25) we have defined two Courant-Friedrichs-Lewy numbers, one for convection $CFL_{adv} = \frac{(1+\frac{1}{Ma})\Delta t}{\Delta x}$ and one for diffusion $CFL_{diff} = \frac{\Delta t}{Re\Delta x^2}$. We can thus define a final CFL as $CFL = \max(CFL_{adv}, CFL_{diff})$: from a user point of view, this is the interesting quantity since it determines the maximum Δt allowed for a l_2 numerically stable simulation. Please note also that the correct quantity used to compare the number of operations performed by two different ERK methods (and therefore assess their efficiency) is not the CFL itself but the *reduced CFL*, which is defined as $CFL_r = \frac{CFL}{s}$, that is the CFL divided by the number of stages.

4.3. Optimized ERK method for low Mach number

In the case of low Mach number regimes, the spectrum looks like an ellipse whose major semi-axis is along the imaginary axis but slightly shifted into the stable side of the complex plane. For this configuration we have considered two approaches which are here denoted as *Option A* and *Option B*. *Option A* consists in choosing the exact spectrum of the semi-discretization corresponding to $Ma = 0.01$ and $Re = 1000$, displayed in Fig. 2, whereas *Option B* solves problem (Eq. (22)) for a circumscribed rectangle of the spectrum that also contains the imaginary axis. We determine optimized stability regions for two orders of accuracy $p = 3$ (resp. $p = 4$), for a dissipative order $q = 3$ (resp. $q = 3$) and for a dispersive order $r = 4$ (resp. $r = 6$).

Fig. 3 displays the reduced absolute stability region for $p = 3$ and $p = 4$ for *Option A* for a number of stages $s \in [p+1, 10]$. We denote *reduced absolute stability region*, the region S/s, that is homothetic to the region S by a factor $\frac{1}{s}$. In other words, as stated above, the interesting quantity to look at is not the CFL number but *the reduced CFL number* $\frac{CFL}{s}$. In Fig. 3 it is possible to observe two main trends. As the number of stages increases, the stability limit in the real axis is reduced but the stability limit in the imaginary axis increases. Since $\frac{CFL_{adv}}{s}$ is the strictest criteria, then the global CFL is increased as the number of stages increases.

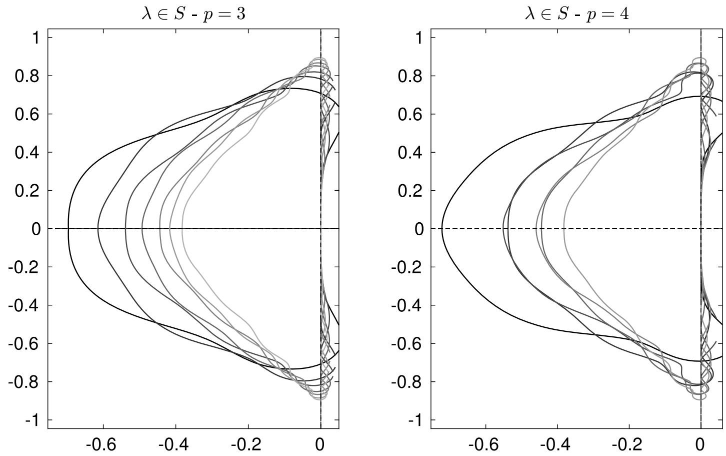

Fig. 4. *Option B*. Scaled absolute stability region with respect to the number of stages for the low Mach number case. On the left (resp. right) the stability region for several ERK schemes of order $p = 3$ (resp. $p = 4$) is displayed. Same legend as in Fig. 3.

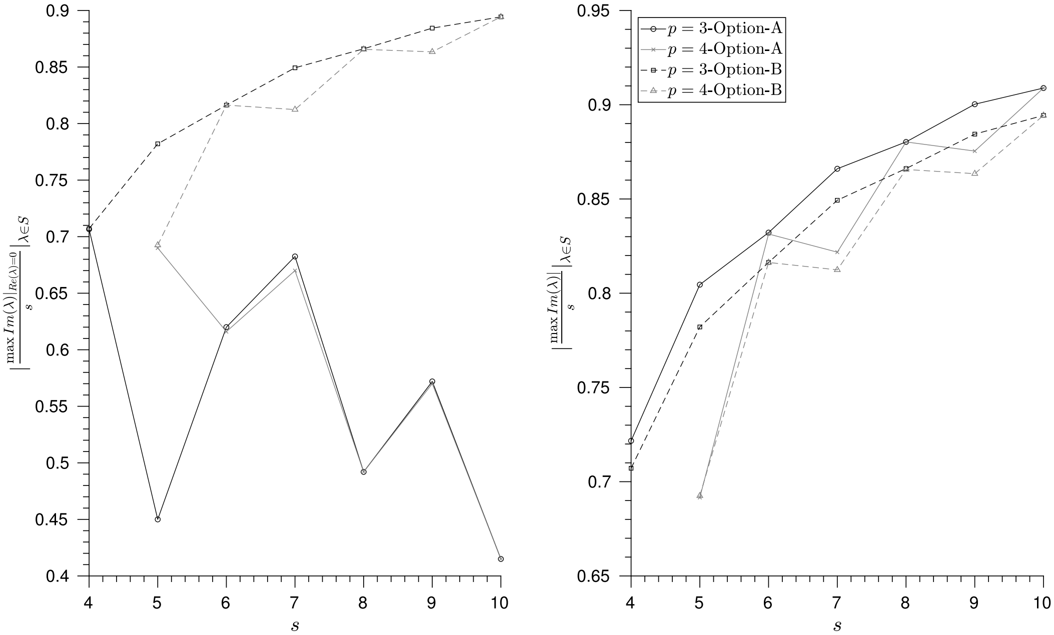

Fig. 5. On the left it is displayed the reduced maximum stability gap $\frac{\max Im(\lambda)}{s}|_{Re(\lambda)=0}$ at the imaginary axis. *Option A* is denoted with solid lines whereas dashed lines denote *Option B*. On the right the maximum reduced imaginary gap $\frac{\max Im(\lambda)}{s}|$ is displayed with the legend as on the left.

However, Fig. 3 also shows that as the number of stages are increased, the reduced absolute stability region starts to wiggle around the imaginary axis. Therefore, time-integration schemes optimized with *Option A* will be efficient for near design configurations but we do not expect them to be robust for other configurations dominated by advection effects. *Option B* has been selected to design a more robust time-stepping algorithm which is efficient not only for low and moderate Reynolds numbers but also for high values of Re.

Fig. 4 displays the reduced absolute stability region once again for $p = 3$ and $p = 4$ for a number of stages $s \in [p + 1, 10]$. In Fig. 4 it is again possible to observe the same two main trends as in Fig. 3. However, in this case the stability region does not oscillate around the imaginary axis, which means that the selected method is robust and efficient also in the limit $Re \to \infty$.

A comparison between *Option A* and *Option B* is summarized in Fig. 5. Solid lines are used for *Option A* whereas dashed lines denote *Option B*. At the left of Fig. 5 it is possible to observe that for *Option B* the maximum CFL for $Re \to \infty$ increases as the number of stages increases, whereas for *Option A* the CFL is limited by the oscillations of the stability region around the imaginary axis. Similarly, the maximum CFL that fits the designed spectrum at low Ma increases

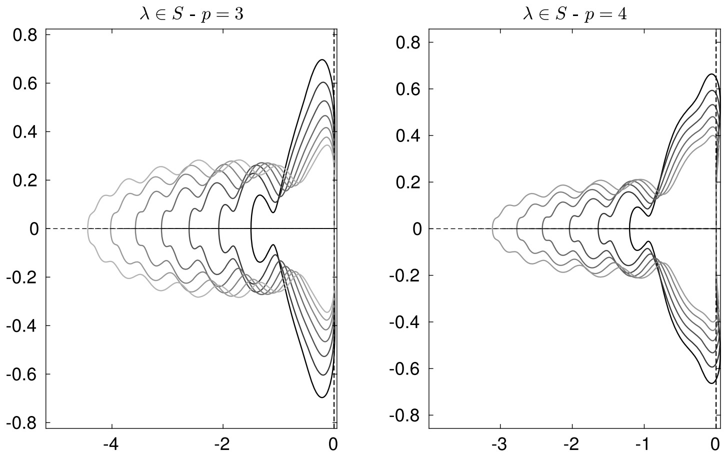

Fig. 6. Scaled absolute stability region with respect to the number of stages for the low Mach number case. On the left (resp. right) the stability region for several ERK schemes of order $p = 3$ (resp. $p = 4$) is displayed. Contours correspond to different numbers of stages $s = [p+1, 10]$, with lighter gray scale indicating an higher number of stages. Dot-dashed curves correspond to the designed spectrum which corresponds to the case displayed in Fig. 2.

for both options as the number of stages increases. Then, *Option B* seems to be sub-optimal for this problem but with wider applications. This is the reason that led us to select ERK(10,3) B and ERK(10,4) B.

4.4. Optimized ERK method for moderate Mach and low Re

In the case of low Reynolds numbers and moderate Mach numbers, regimes of interest in the study of transitional flows (see e.g. [8] [10] [7]), the shape of the spectrum is still an ellipse but with its major semi-axis aligned now along the real axis. In the design case $Re = 100$ and $Ma = 0.4$, CFL_{diff} seems to be the dominant CFL since the ratio $\frac{a}{b}$ of major semi-axis a and minor semi-axis b of the ellipse is $O(10^1)$ for both $\mathbb{P}^1$ and $\mathbb{P}^2$ discretizations. We determine the maximum stability regions for an order of accuracy $p = 3$ (resp. $p = 4$), dissipative order $q = 3$ (resp. $q = 3$) and dispersive order $r = 4$ (resp. $r = 6$).

In this case Fig. 6 displays the optimal reduced stability region for $s \in [p+1, 10]$ for $p = 3, 4$.

Fig. 7 shows the stability characteristics for the chosen configuration. It is observed that $\frac{\max Re(\lambda)}{s}$ for a fixed Δt increases with the number of stages s or, equivalently, that the reduced diffusive CFL number $\frac{CFL_{diff}}{s}$ increases with s, whereas $\frac{\max Im(\lambda)|_{Re(\lambda)=0}}{s}$ decreases with the number of stages s. Similarly, the minimum reduced imaginary gap $\frac{\min Im(\lambda)}{s}$ seems to be constant or even slightly increases with the number of stages. In any case this quantity should not be of much importance for sufficiently diffusive configurations, i.e. for sufficiently low Re.

5. Numerical experiments

5.1. Verification of order of accuracy

In this section we show a convergence study of optimized ERK methods with respect to some classic ERK methods of orders $p = 3, 4$. We consider two cases, a linear test case and a nonlinear stiff problem with chaotic dynamics.

Linear system. We consider a simple linear ordinary differential equation

$$\frac{d}{dt}u(t) = u(t) \quad \text{and} \quad u(0) = 1 \tag{26}$$

whose analytical solution is simply $u(t) = e^t$.

The order of accuracy is computed by marching in time (Eq. (26)) until $T = 10$ with several classic ERK and with optimized ERK, such as ERK(4,4) or ERK(3,3), shown in Section 4.3 and Section 4.4. The convergence diagram for the optimized ERK(10,3) Option B (resp. ERK(10,4) B) is compared with those of other classic ERK schemes on the left of figure (Fig. 8): results show that each of the optimized ERK schemes converges with the expected order of accuracy. A comparison among different optimized ERK schemes for $p = 3, 4$ is further documented on the left of figure (Fig. 9).

Nonlinear system. The Lorenz system is a simplified mathematical model for atmospheric convection, first derived by Edward Lorenz in 1963. It consists of the following set of three ordinary differential equations

$$\frac{dq_1}{dt} = \sigma(q_2 - q_1) \tag{27a}$$

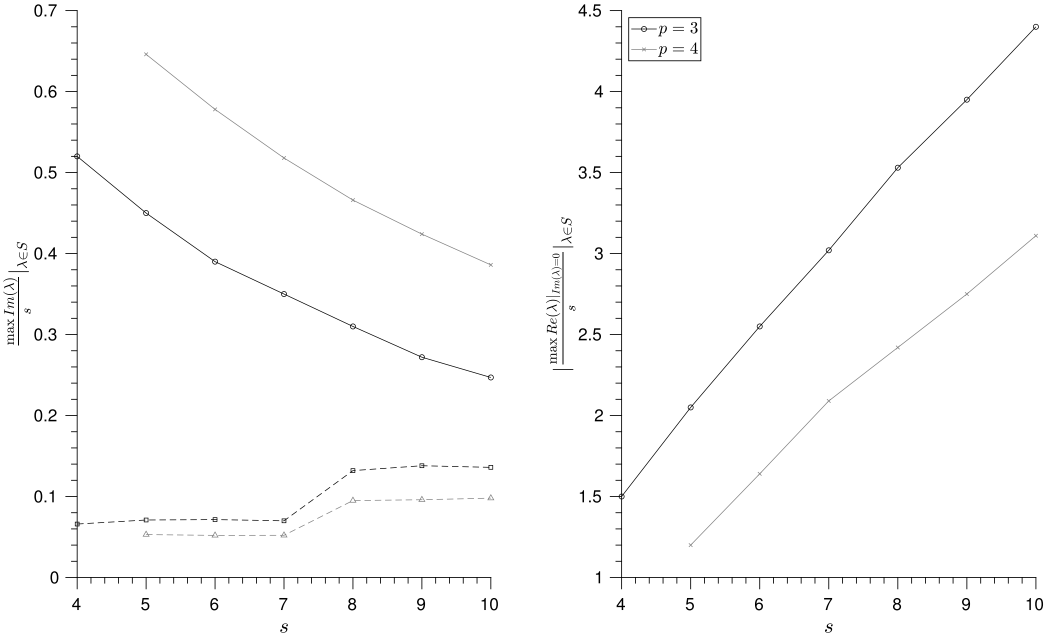

Fig. 7. Left figure: reduced maximum imaginary stability gap $\frac{\max Im(\lambda)}{s}|$ (▬) and minimum stability gap on the imaginary axis $\frac{\min Im(\lambda)}{s}|$ (- - -). Right figure: maximum reduced real stability gap $\frac{\max Re(\lambda)}{s}|_{Im(\lambda)=0}$. Black and gray lines denote the $p = 3$ and $p = 4$ case respectively.

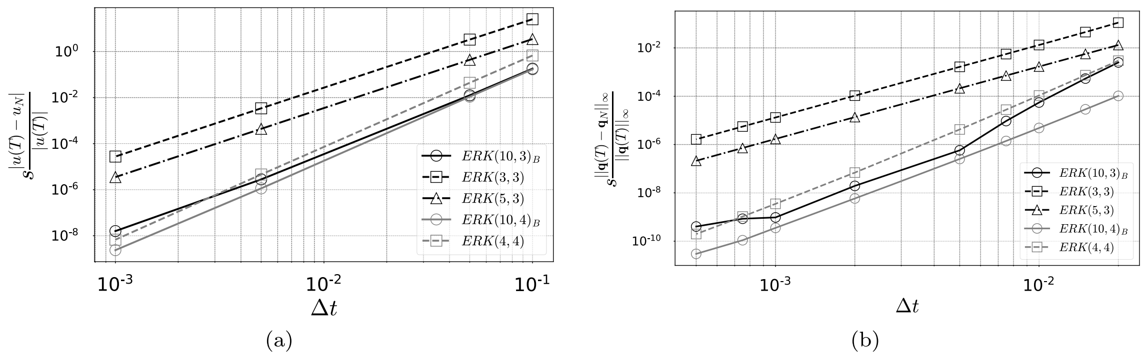

Fig. 8. Comparison of ERK or order $p = 3, 4$ where black lines are used to denote third order and gray for fourth order. Classic $ERK(3, 3)$, $ERK(5, 3)$, $ERK(4, 4)$, and Option B optimized schemes for low Mach number. Order of accuracy for the linear problem on the left and for the non-linear one on the right.

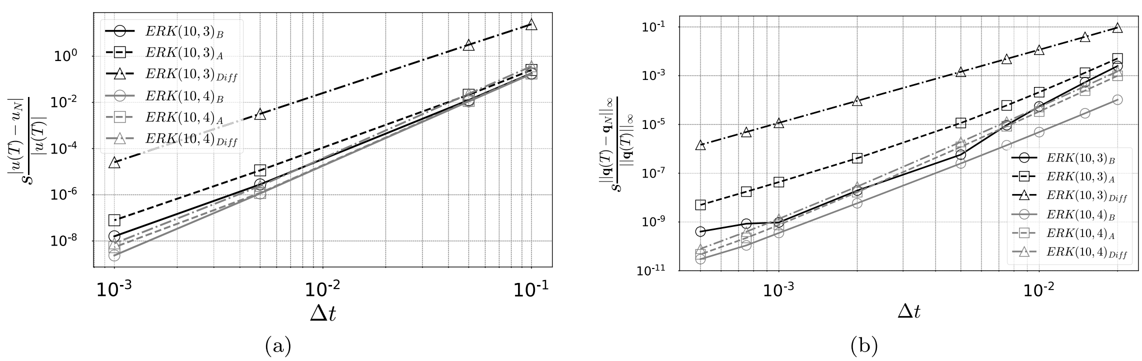

Fig. 9. It is displayed a comparison of ERK or order $p = 3, 4$ where black lines are used to denote third order and gray for fourth order. Optimized ERK (Option A and B) for low Mach number and for moderate *Ma* and low *Re*, here denoted as *Diff*. Order of accuracy for the linear problem on the left and for the non-linear one on the right.

Table 3
Numerical determination of the stability limit for the advection-diffusion equation.

ERK method	Case 1 – $\frac{CFL_{\max}}{s}$	Case 2 – $\frac{CFL_{\max}}{s}$
ERK(10, 4) A	0.402	–
ERK(10, 4) B	0.513	–
ERK(10, 4) Diff	–	0.256
ERK(4, 4)	0.405	0.0575
ERK(10, 3) A	0.402	–
ERK(10, 3) B	0.512	–
ERK(10, 3) Diff	–	0.3625
ERK(5, 3)	0.402	0.062
ERK(3, 3)	0.34	0.06925

$$\frac{dq_2}{dt} = q_1(\rho - q_3) - q_2 \tag{27b}$$

$$\frac{dq_3}{dt} = q_1 q_2 - \beta q_3 \tag{27c}$$

The equations relate the properties of a two-dimensional fluid layer uniformly heated from below and cooled from above. In particular, the equations describe the rate of change of three quantities with respect to time: x is proportional to the rate of convection, y to the horizontal temperature variation and z to the vertical temperature variation. The system is known for having chaotic solutions for certain parameter values and initial conditions [18]. This system is integrated here using the initial condition $\mathbf{q}(0) = [5, -5, 20]$ and the following values for the parameters: $\sigma = 10$, $\rho = 28$ and $\beta = \frac{8}{3}$. Such choice corresponds to a chaotic dynamics. The relative error $\frac{||\mathbf{q}(T) - \mathbf{q}_N||_\infty}{||\mathbf{q}(T)||_\infty}$, is evaluated with respect to $\mathbf{q}(T)$ which has been computed with ERK(4,4) with a Δt a thousand times smaller than the smallest Δt used to determine the order of accuracy. On the right of figures (Fig. 8) and (Fig. 9) convergence diagrams for the Lorentz problem are displayed with the same legend as used in the linear ODE case. Every tested ERK method shows the expected order of accuracy. However, convergence trend of ERK(10,3) B is not exactly as expected: at high values of Δt the scheme seems to have a higher order of accuracy whereas at lower values of Δt convergence degrades due to round-off errors (note in fact that the error is under the square root of machine precision).

5.2. Linear advection-diffusion equation

We now consider the linear advection-diffusion equation (Eq. (23a)). In the present section we show the effectiveness of the optimized ERK schemes for two different regimes:

- **Case 1**: low Mach number and high Reynolds number flows, $Ma = 0.01$ and $Re = 10^5$
- **Case 2**: moderate Mach numbers, $Ma = 0.4$ and low Reynolds number, $Re = 100$.

$\mathbb{P}_1$ Lagrange elements are considered for the spatial semi-discretization and ERK schemes are used for time integration. Results are displayed in Table 3. As expected, oscillations of the absolute stability region boundary near the imaginary axis for the method ERK(10,$p = 3, 4$) A lead to an efficiency approximately 25% smaller than ERK(10,$p = 3, 4$) B. ERK(10,$p = 3, 4$) B is also around 25% more efficient than classic ERK, such as ERK(4,4) or ERK(5,3) respectively. On the other hand, for **Case 2** the optimized ERK(10,$p = 3, 4$) has a reduced CFL $\frac{CFL_{\max}}{s}$ around five times higher than classic third or fourth order ERK schemes. The main reason of that performance difference is due to the fact that classic ERK are generally designed to have a wide absolute stability region along the imaginary axis. Furthermore, due to a classical CFL theorem [36], the reduced CFL number for convection dominated problems has to be $\frac{CFL_{adv,\max}}{s} < 1$. Basically, we conclude that the optimal gain in stability is obtained with relatively low stages for advection dominated problems whereas for diffusion dominated cases it is possible to increase even more the stability gap. However, we decided not to go beyond $s = 10$ due to memory requirements of large-scale problems and to provide more robustness to the ERK method, so it can deal with a wider interval of Re.

5.3. Compressible Navier-Stokes equations

In this section we consider the motion of a compressible fluid. The system is described by the usual compressible Navier-Stokes equations, $\mathbf{B}\frac{\partial \mathbf{q}}{\partial \mathbf{t}} + \mathcal{NS}(\mathbf{q}) = 0$. Since we focus on subsonic flows, we use a non-conservative formulation of the governing equations, with the state vector given by $\mathbf{q} = [\rho, \mathbf{u}, T, p]$. The system state is described by the velocity field $\boldsymbol{u}(\boldsymbol{x}, t)$, the pressure $p(\boldsymbol{x}, t)$, the fluid density field $\rho(\boldsymbol{x}, t)$ and the temperature $T(\boldsymbol{x}, t)$ which satisfy the unsteady compressible Navier-Stokes equations:

$$\frac{\partial \rho}{\partial t} + \mathbf{u} \cdot \nabla \rho + \rho \nabla \cdot \mathbf{u} = 0, \tag{28a}$$

Table 4
Numerical determination of the stability limit for the flow past a fixed cylinder for $Re = 100$ and $Ma = 0.01$. $\frac{CFL_{adv}}{s}$ is being defined in Eq. (25). η is the ratio of the reduced $CFL_r = \frac{CFL_{adv}}{s}$ of each ERK method with that of ERK(10, 4) B.

ERK method	$\frac{CFL_{adv}}{s}$	η
ERK(10, 4) A	0.151	0.993
ERK(10, 4) B	0.152	1
ERK(4, 4)	0.132	0.868
ERK(10, 3) A	0.15	0.987
ERK(10, 3) B	0.151	0.993
ERK(3, 3)	0.143	0.94

$$\rho\frac{\partial \mathbf{u}}{\partial t} + \rho\mathbf{u}\cdot\nabla\mathbf{u} + \nabla p - \frac{1}{Re}\tau(\mathbf{u}) = \mathbf{0}, \tag{28b}$$

$$\rho\frac{\partial T}{\partial t} + \rho\mathbf{u}\cdot\nabla T + (\gamma-1)\rho T\nabla\cdot\mathbf{u} - \gamma(\gamma-1)\frac{Ma^2}{Re}\tau(\mathbf{u}):\mathbf{d}(\mathbf{u}) - \frac{\gamma}{Pr\,Re}\nabla^2 T = 0, \tag{28c}$$

$$\rho T - 1 - \gamma Ma^2 p = 0, \tag{28d}$$

where γ is the ratio of specific heats (here equal to 1.4), $\mathbf{d}(\mathbf{u}) = \frac{1}{2}\left(\nabla\mathbf{u} + \nabla\mathbf{u}^T\right)$ is the strain tensor and $\tau(\mathbf{u}) = [2\mathbf{d}(\mathbf{u}) - \frac{2}{3}(\nabla\cdot\mathbf{u})\mathbf{I}]$ is the stress tensor per unit viscosity. Here, we assume that viscosity and the thermal conductivity of the fluid are constant and independent of the temperature.

In particular, the classic two-dimensional flow past a circular cylinder (see e.g. [38] and [17]) at low Re has been considered here as a test problem. Equations (28) are made non-dimensional by using the cylinder diameter D as length scale and the upstream quantities U_∞, ρ_∞, T_∞; the dimensionless pressure is defined as $\frac{p-p_\infty}{\rho_\infty U_\infty^2}$. Thus, the Reynolds ($Re$) and Mach ($Ma$) numbers are defined as:

$$Re = \frac{\rho_\infty U_\infty D}{\mu}, \quad Ma = \frac{U_\infty}{\sqrt{\gamma R T_\infty}}$$

where R is the ideal gas constant. These equations have been used to test the performances of the optimized ERK(s, p) schemes described above. The spatial discretization of these equations has been carried out using $\mathbb{P}_2$ elements for the velocity field $\mathbf{u}$ and $\mathbb{P}_1$ elements for ρ, T, p, so that the inf – sup condition is satisfied in the incompressible limit $M \to 0$, [22]. Equations (Eq. (28)) are complemented with standard boundary conditions for this configuration [16]: adiabatic and no-slip boundary conditions are considered for the cylinder surface, while uniform velocity $\mathbf{u} = [U_0, 0]$, temperature T_0 and density ρ_0 are imposed at the inlet. An unstructured nonuniform triangular mesh has been generated with a Delaunay algorithm. In order to avoid spurious reflections of acoustic waves, a sponge zone has been introduced to damp the perturbations before they reach the boundaries of the computational domain. Here we followed the same approach as proposed by Rowley et al. [35] and successfully used in [16].

Once again, we have considered two regimes with a fixed Reynolds number $Re = 100$ and different Ma numbers:

- **Case 1**: low Mach number ($Ma = 0.01$): the stability limit for this case is displayed in Table 4. It is observed that ERK(10, 4) B is the most efficient forth order method among the considered schemes: results show that it is approximatively 15% more efficient than the classic fourth-order Runge-Kutta method. Lower gain is instead obtained for the optimized third-order ERK scheme, which results only 5% more efficient than the classic $ERK(3, 3)$. The difference in efficiency observed in this test case and in the linear advection-diffusion benchmark may be explained by the fact that the considered Re is here much lower than in Section 5.2.
- **Case 2**: moderate Mach number, $Ma = 0.4$. In this regime the stability limit for four ERK methods have been assessed: more precisely we have analyzed the performances of the two optimized methods for moderate Mach numbers, ERK(10, p) Diff and the two classical ERK methods of order three and four with the same number of stages. It is observed (see Table 5) that optimized schemes are around four (resp. five) times more efficient than the classical fourth (resp. third) order schemes. So indeed, we were able to recover a stability gain similar to that obtained for the linear advection-diffusion equation.
- **Comparison with [20]**: Finally, we compare our results against the DNS data presented by [20]. Fig. 10 shows the contour plot of a snapshot of the vorticity field for a Reynolds number $Re = 150$ and a Mach number $Ma = 0.2$. We chose these parameters to provide a direct comparison against the results documented by [20]. Fig. 11 depicts the directivity pattern computed by using our optimized ERK scheme. We observe an excellent agreement between our data and the data obtained by [20]. This comparison validates our numerical setting and confirms that the proposed methodology is suitable to design optimal Explicit Runge-Kutta methods for compressible flow simulations.

Table 5
Numerical determination of the stability limit for the flow past a fixed cylinder for $Re = 100$ and $Ma = 0.4$. $\frac{CFL_{diff}}{s}$ and $\frac{CFL_{adv}}{s}$ are being defined in Eq. (25). η is the ratio of $\frac{CFL_{adv}}{s}$ of each ERK method with respect to ERK(10, 3) Diff.

ERK method	$\frac{CFL_{diff}}{s}$	$\frac{CFL_{adv}}{s}$	η
ERK(10, 4) Diff	0.0168	0.077	0.6875
ERK(4, 4)	0.00415	0.019	0.17
ERK(10, 3) Diff	0.0245	0.112	1
ERK(3, 3)	0.0048	0.022	0.2

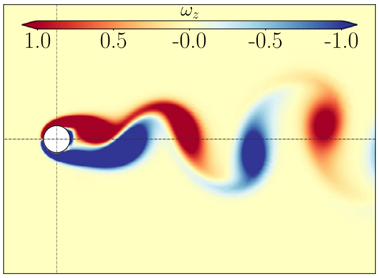

Fig. 10. Instantaneous contour plot of the vorticity $\omega_z = \partial_x v - \partial_y u$ in the flow past a circular cylinder at $Re = 150$ and $M = 0.2$. (For interpretation of the colors in the figure, the reader is referred to the web version of this article.)

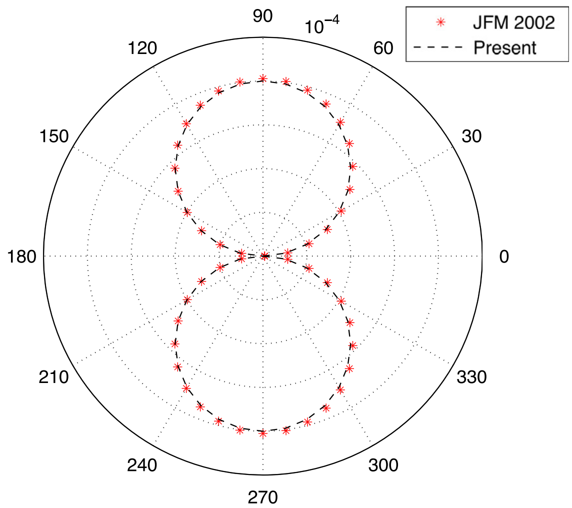

Fig. 11. Directivity pattern based on the root mean square (RMS) values of the disturbance pressure ΔP^M (see Inoue & Hatakeyama [20] for further details) evaluated at $r = 75$.

Remark. Please note that numerical codes for the compressible Navier-Stokes equations have been written in FreeFEM++ and they belong to a project called StabFem (https://gitlab.com/stabfem/StabFem). Further details can be found in [15].

6. Conclusion

In this paper we analyze the performances of explicit Runge-Kutta methods designed for the numerical simulations of compressible fluid flows when a finite element approximation is used in space. In particular, we have focused our attention on the determination of more efficient time-stepping methods in cases where stability is a limiting factor. The methodology adopted is similar to the one described in [24] and [29], but with the imposition of extra conditions on the order of the dispersive and dissipative errors. In our study, we considered two different regimes, the acoustic problem at low Mach numbers and the subsonic regime. For the former we have determined an explicit fourth-order Runge-Kutta method ERK(10, 4) B that is around 15% more efficient than classical ERK(4, 4) schemes. The low gain is due to the fact that the absolute stability region near the imaginary axis cannot extend over values larger than the number of adopted stages [36] while the region of absolute instability for ERK(4, 4) already crosses the imaginary axis at around three. For moderate Mach numbers, around $Ma = 0.4$, and for transitional Reynolds numbers, we have determined ERK schemes that outperform classic ERK(3, 3) or

ERK(4, 4) schemes. Optimal ERKs have a reduced CFL, $\frac{CFL_{max}}{s}$, which is approximately four or five times larger than that of the classical ones. We would like to remark here that, even though they were designed for the compressible Navier-Stokes equations, the optimized ERK schemes can be used to solve the incompressible Navier-Stokes equations too. In particular ERK(10,4) B is efficient for large *Re* regimes and ERK(10,4) Diff is efficient for transitional flows (see Tables A.6–A.11). In particular, the former could be used for turbulent simulations whereas the latter is suited for global stability studies like [6], [14] or for non-modal transient growth analysis [37]. The effectiveness of the proposed approach will also be tested in the case of PDEs generating periodic wavefronts [3,12,11].

Appendix A. Optimized ERK methods

Table A.6
ERK(10, 4) A.

0										
−0.027 135 6	−0.027 135 6	0	0	0	0	0	0	0	0	0
$8.853\,690\,9\cdot10^{-4}$	0.183 507 7	−0.182 622 4	0	0	0	0	0	0	0	0
0.147 525 8	−0.140 474 1	−0.177 159 8	0.465 159 7	0	0	0	0	0	0	0
0.094 796 2	−0.050 333 0	−0.242 519 5	0.420 919 6	−0.033 270 8	0	0	0	0	0	0
0.089 435 4	−0.358 449 7	0.029 229 4	0.587 521 1	0.353 107 0	−0.521 972 3	0	0	0	0	0
0.318 118 5	0.007 678 1	−0.419 034 8	0.367 269 4	0.123 856 2	0.024 069 2	0.214 280 4	0	0	0	0
0.678 340 9	−0.223 694 9	−0.068 303 4	−0.118 928 3	0.174 393 5	−0.248 796 7	0.601 980 0	0.561 690 5	0	0	0
0.281 465 6	0.018 861 4	−0.021 965 4	0.147 501 0	0.320 470 1	−0.569 420 9	0.379 744 8	−0.011 688 2	0.017 962 9	0	0
0.786 340 1	−0.149 351 7	0.125 867 2	0.011 105 1	−0.165 870 4	−0.173 357 2	0.188 117 3	−0.217 173 1	0.201 237 2	0.965 765 6	0
	0.154 955 9	0.157 516 3	−0.208 559 0	−0.393 698 9	0.270 636 5	−0.112 714 7	0.694 502 9	−0.434 758 7	0.128 422 5	0.743 697 2

Table A.7
ERK(10, 4) B.

0										
−0.169 055 1	−0.169 055 1	0	0	0	0	0	0	0	0	0
−0.129 423 5	−0.191 620 5	0.062 197 0	0	0	0	0	0	0	0	0
0.323 537 5	0.078 539 8	0.081 634 9	0.163 362 8	0	0	0	0	0	0	0
0.114 741 9	−0.087 930 1	0.394 868 1	0.068 335 2	−0.260 531 3	0	0	0	0	0	0
0.694 858 7	−0.649 494 9	0.248 959 5	0.129 550 0	0.935 519 4	0.030 324 7	0	0	0	0	0
−0.137 376 0	0.603 289 8	−0.246 570 8	−0.040 638 5	0.115 065 7	−0.448 529 4	−0.119 992 7	0	0	0	0
0.795 318 8	−0.262 135 0	−0.184 203 3	0.183 618 0	0.443 782 5	1.066 689 2	−0.082 257 2	−0.370 175 3	0	0	0
0.609 893 4	0.004 387 6	−0.088 987 8	−0.439 656 6	0.271 469 2	0.405 286 4	−0.278 442 6	0.553 330 9	0.182 506 3	0	0
0.756 180 5	0.082 149 4	−0.263 782 9	−0.026 276 4	0.123 592 5	0.324 501 9	0.209 638 1	0.178 120 2	−0.234 658 0	0.362 895 7	0
	0.394 655 2	−0.078 540 2	−0.042 604 6	0.457 003 6	−0.157 466 1	−0.838 506 6	0.009 545 0	−0.464 757 4	−0.026 425 6	1.747 096 8

Table A.8
ERK(10, 4) Diff.

0										
0.040 391 5	0.040 391 5	0	0	0	0	0	0	0	0	0
0.098 029 9	0.063 878 9	0.034 150 9	0	0	0	0	0	0	0	0
−0.000 727 6	0.184 279 3	−0.088 424 8	−0.096 582 1	0	0	0	0	0	0	0
0.357 482 6	−0.167 629 3	0.175 354 0	0.482 347 4	−0.132 589 6	0	0	0	0	0	0
0.184 624 6	−0.343 957 6	−0.055 090 7	0.122 665 2	0.448 549 7	0.012 458 1	0	0	0	0	0
0.625 733 3	0.316 930 9	−0.026 363 7	−0.281 840 2	−0.078 996 7	0.528 216 6	0.167 786 3	0	0	0	0
0.043 289 8	−0.485 801 6	0.269 465 6	−0.326 692 6	0.527 705 7	0.537 150 7	−0.356 288 2	−0.122 249 7	0	0	0
0.234 980 8	−0.298 297 2	0.435 746 5	0.573 560 0	0.240 223 1	−0.067 239 3	−0.146 649 5	0.154 191 6	−0.656 554 2	0	0
0.912 271 2	−0.036 051 7	0.611 309 4	−0.032 747 7	−0.020 105 8	−0.071 125 6	−0.270 435 8	0.685 447 0	−0.173 112 5	0.219 093 9	0
	0.656 836 2	0.482 735 4	−0.147 142 1	−0.608 029 6	0.094 187 9	0.285 917 9	0.339 041 0	−0.405 146 0	0.091 135 8	0.210 463 5

Table A.9
ERK(10, 3) A.

0										
−0.031 810 9	−0.031 810 9	0	0	0	0	0	0	0	0	0
−0.019 878 9	0.124 226 3	−0.144 105 2	0	0	0	0	0	0	0	0
0.049 886 8	0.154 884 6	−0.174 694 9	0.069 697 1	0	0	0	0	0	0	0
0.155 850 9	0.068 678 2	−0.272 093 1	0.062 946 3	0.296 319 5	0	0	0	0	0	0
0.432 093 1	−0.209 884 4	−0.245 119 3	0.002 356 4	0.383 286 7	0.501 453 8	0	0	0	0	0
0.070 433 3	0.393 998 8	0.039 487 9	0.172 809 4	−0.209 004 2	0.104 055 5	−0.430 914 2	0	0	0	0
0.555 696 4	0.619 908 3	−0.093 383 4	−0.056 717 3	−0.065 948 2	0.068 140 5	−0.109 570 0	0.193 266 6	0	0	0
0.167 841 9	0.301 509 8	0.142 546 9	0.050 666 5	0.140 130 3	−0.115 427 1	−0.092 313 8	−0.189 550 2	−0.069 720 4	0	0
0.690 781 4	−0.045 251 1	0.003 360 7	0.106 533 9	0.237 586 6	0.320 889 3	−0.223 794 0	−0.255 870 9	0.344 311 5	0.203 015 5	0
	−0.384 961 9	0.280 551 7	−0.160 324 0	0.045 731 8	0.573 697 8	−0.163 792 1	−0.066 138 1	−0.594 990 0	0.373 836 2	1.096 388 7

Table A.10
ERK(10, 3) B.

0										
−0.149 984 4	−0.149 984 4	0	0	0	0	0	0	0	0	0
0.071 835 4	−0.223 813 7	0.295 649 1	0	0	0	0	0	0	0	0
−0.023 312 7	0.357 889 6	−0.111 108 8	−0.270 093 6	0	0	0	0	0	0	0
−0.125 845 0	0.401 676 6	−0.195 421 8	−0.205 459 8	−0.126 640 0	0	0	0	0	0	0
−0.096 574 1	−0.113 566 2	−0.156 284 3	0.158 936 8	−0.017 038 2	0.031 377 8	0	0	0	0	0
0.211 369 2	0.426 256 1	−0.291 572 5	0.254 475 8	0.125 500 4	−0.087 521 9	−0.215 768 7	0	0	0	0
0.620 134 7	0.494 478 2	0.176 859 2	0.077 548 5	−0.158 373 2	−0.175 275 8	−0.090 414 7	0.295 312 4	0	0	0
0.274 302 8	0.218 300 1	−0.373 042 4	0.087 314 7	0.718 075 1	−0.422 973 6	0.099 566 8	−0.099 370 7	0.046 432 7	0	0
0.695 748 1	−0.158 985 7	0.002 072 9	0.157 330 7	0.002 748 6	0.445 000 1	−0.368 528 3	0.158 017 8	0.077 621 4	0.380 470 7	0
	−0.310 413 8	−0.031 587 7	0.498 570 4	0.170 792 9	−0.205 866 7	0.194 805 8	−0.018 616 2	−0.810 806 6	0.212 774 1	1.300 347 9

Table A.11
ERK(10, 3) Diff.

0										
0.002 183 3	0.002 183 3	0	0	0	0	0	0	0	0	0
−0.008 879 9	0.087 540 5	−0.096 420 4	0	0	0	0	0	0	0	0
−0.177 394 5	−0.276 824 4	0.443 730 1	−0.344 300 2	0	0	0	0	0	0	0
0.344 315 0	0.033 946 7	0.245 344 0	0.060 901 2	0.004 123 0	0	0	0	0	0	0
0.207 858 5	−0.380 921 3	−0.363 714 5	0.460 254 1	0.162 146 8	0.330 093 5	0	0	0	0	0
−0.087 843 8	−0.028 331 9	−0.053 160 7	−0.570 454 2	0.435 568 1	0.078 856 5	0.049 678 4	0	0	0	0
0.102 743 0	−0.015 985 9	−0.455 873 4	−0.100 894 4	−0.212 554 3	0.263 200 0	0.543 448 5	0.081 402 5	0	0	0
−0.126 928 8	−0.022 261 0	0.259 057 8	0.187 885 1	0.023 628 0	−0.117 904 4	−0.270 273 0	−0.228 403 3	0.041 342 0	0	0
0.486 132 6	−0.047 270 9	0.073 228 3	−0.490 253 9	−0.023 703 3	0.337 245 1	0.315 034 9	−0.002 806 3	0.070 021 5	0.254 637 2	0
	−0.213 878 3	−0.412 134 3	0.107 428 2	0.027 715 3	−0.401 949 3	−0.285 847 5	0.634 198 4	−0.217 623 6	0.120 635 5	1.641 455 7

References

[1] P. Albrecht, The Runge–Kutta theory in a nutshell, SIAM J. Numer. Anal. 33 (5) (1996) 1712–1735.
[2] J.C. Butcher, J. Butcher, The Numerical Analysis of Ordinary Differential Equations: Runge-Kutta and General Linear Methods, Vol. 512, Wiley, New York, 1987.
[3] A. Cardone, R. D'Ambrosio, B. Paternoster, Exponentially fitted IMEX methods for advection-diffusion problems, J. Comput. Appl. Math. 316 (2017) 100–108.
[4] S. Chakravarthy, S. Osher, A new class of high accuracy TVD schemes for hyperbolic conservationlaws, in: 23rd Aerospace Sciences Meeting, 1985, p. 363.
[5] V. Citro, Simple and efficient acceleration of existing multigrid algorithms, AIAA J. 57 (6) (2019) 2244–2247.
[6] V. Citro, F. Giannetti, P. Luchini, F. Auteri, Global stability and sensitivity analysis of boundary-layer flows past a hemispherical roughness element, Phys. Fluids 27 (8) (2015) 084110.
[7] V. Citro, F. Giannetti, J. Pralits, Three-dimensional stability, receptivity and sensitivity of non-Newtonian flows inside open cavities, Fluid Dyn. Res. 47 (2015) 1–14.
[8] V. Citro, J. Tchoufag, D. Fabre, F. Giannetti, P. Luchini, Linear stability and weakly nonlinear analysis of the flow past rotating spheres, J. Fluid Mech. 807 (2016) 62–86.
[9] V. Citro, P. Luchini, F. Giannetti, F. Auteri, Efficient stabilization and acceleration of numerical simulation of fluid flows by residual recombination, J. Comput. Phys. 344 (1) (2017) 234–246.
[10] V. Citro, L. Siconolfi, D. Fabre, F. Giannetti, P. Luchini, Stability and sensitivity analysis of the secondary instability in the sphere wake, AIAA J. 55 (2017) 3661–3668.
[11] R. D'Ambrosio, B. Paternoster, Numerical solution of reaction-diffusion systems of lambda-omega type by trigonometrically fitted methods, J. Comput. Appl. Math. 294 (2016) 436–445.
[12] R. D'Ambrosio, M. Moccaldi, B. Paternoster, Adapted numerical methods for advection-reaction-diffusion problems generating periodic wavefronts, Comput. Math. Appl. 74 (2017) 1029–1042.
[13] E.D. de Goede, Stabilization of the Lax-Wendroff method and a generalized one-step Runge-Kutta method for hyperbolic initial-value problems, Appl. Numer. Math. 4 (5) (1988) 439–453.
[14] D. Fabre, J. Tchoufag, V. Citro, F. Giannetti, P. Luchini, The flow past a freely rotating sphere, Theor. Comput. Fluid Dyn. 31 (5–6) (2017) 475–482.
[15] D. Fabre, V. Citro, D.F. Sabino, P. Bonnefis, J. Sierra, F. Giannetti, M. Pigou, A practical review on linear and nonlinear global approaches to flow instabilities, Appl. Mech. Rev. 70 (6) (2018).
[16] A. Fani, V. Citro, F. Giannetti, F. Auteri, Computation of the bluff-body sound generation by a self-consistent mean flow formulation featured, Phys. Fluids 30 (3) (2018) 036102.
[17] F. Giannetti, S. Camarri, V. Citro, Sensitivity analysis and passive control of the secondary instability in the wake of a cylinder, J. Fluid Mech. 864 (2019) 45–72.
[18] J. Guckenheimer, R.F. Williams, Structural stability of Lorenz attractors, Publ. Math. IHÉS 50 (1979) 59–72.
[19] I. Higueras, T. Roldán, New third order low-storage SSP explicit Runge–Kutta methods, J. Sci. Comput. 79 (3) (2019) 1882–1906.
[20] O. Inoue, N. Hatakeyama, Sound generation by a two-dimensional circular cylinder in a uniform flow, J. Fluid Mech. 471 (2002) 285–314.
[21] L. Isherwood, Z.J. Grant, S. Gottlieb, Strong stability preserving integrating factor Runge–Kutta methods, SIAM J. Numer. Anal. 56 (6) (2018) 3276–3307.
[22] R.B. Kellogg, B. Liu, A finite element method for the compressible Stokes equations, SIAM J. Numer. Anal. 33 (2) (1996) 780–788.
[23] D.I. Ketcheson, Highly efficient strong stability-preserving Runge–Kutta methods with low-storage implementations, SIAM J. Sci. Comput. 30 (4) (2008) 2113–2136.
[24] D.I. Ketcheson, A.J. Ahmadia, Optimal Runge–Kutta Stability Regions, Tech. rep., 2012.
[25] A. Lumsdaine, D. Wu, Spectra and pseudospectra of waveform relaxation operators, SIAM J. Sci. Comput. 18 (1) (1997) 286–304.
[26] J. Mead, R. Renaut, Optimal Runge–Kutta methods for first order pseudospectral operators, J. Comput. Phys. 152 (1) (1999) 404–419.
[27] J. Moulin, P. Jolivet, O. Marquet, Augmented Lagrangian preconditioner for large-scale hydrodynamic stability analysis, Comput. Methods Appl. Mech. Eng. 351 (2019) 718–743.
[28] J. Niegemann, R. Diehl, K. Busch, Efficient low-storage Runge–Kutta schemes with optimized stability regions, J. Comput. Phys. 231 (2) (2012) 364–372.
[29] M. Parsani, D.I. Ketcheson, W. Deconinck, Optimized explicit Runge–Kutta schemes for the spectral difference method applied to wave propagation problems, SIAM J. Sci. Comput. 35 (2) (2013) A957–A986.
[30] B. Paternoster, Runge-Kutta(-Nyström) methods for odes with periodic solutions based on trigonometric polynomials, Appl. Numer. Math. 28 (1998) 401–412.
[31] B. Paternoster, A phase-fitted collocation-based Runge–Kutta–Nyström method, Appl. Numer. Math. 35 (2000) 339–355.
[32] o. Pironneau, Finite Element Methods for Fluids, Chichester etc, Jhon Wiley & Sons, Paris etc., Masson, ISBN 0-471-92255-2, 1989.
[33] R. Rannacher, Finite element methods for the incompressible Navier-Stokes equations, in: Fundamental Directions in Mathematical Fluid Mechanics, Springer, 2000, pp. 191–293.
[34] H. Ranocha, M. Sayyari, L. Dalcin, M. Parsani, D.I. Ketcheson, Relaxation Runge-Kutta methods: fully-discrete explicit entropy-stable schemes for the Euler and Navier-Stokes equations, arXiv:1905.09129.
[35] C.W. Rowley, T. Colonius, A.J. Basu, On self-sustained oscillations in two-dimensional compressible flow over rectangular cavities, J. Fluid Mech. 455 (2002) 315–346.
[36] J.M. Sanz-Serna, M.N. Spijker, Regions of stability, equivalence theorems and the Courant-Friedrichs-Lewy condition, Numer. Math. 49 (2–3) (1986) 319–329.
[37] P.J. Schmid, Nonmodal stability theory, Annu. Rev. Fluid Mech. 39 (2007) 129–162.
[38] L. Siconolfi, V. Citro, F. Giannetti, S. Camarri, P. Luchini, Towards a quantitative comparison between global and local stability analysis, J. Fluid Mech. 819 (2017) 147–164.
[39] G. Strang, Accurate partial difference methods, Numer. Math. 6 (1) (1964) 37–46.
[40] L.N. Trefethen, M. Embree, Spectra and Pseudospectra: the Behavior of Nonnormal Matrices and Operators, Princeton University Press, 2005.
[41] P.J. van der Houwen, B.P. Sommeijer, Explicit Runge–Kutta (–Nyström) methods with reduced phase errors for computing oscillating solutions, SIAM J. Numer. Anal. 24 (3) (1987) 595–617.
[42] M. Wax, T. Kailath, Efficient inversion of Toeplitz-block Toeplitz matrix, IEEE Trans. Acoust. Speech Signal Process. 31 (5) (1983) 1218–1221.